The Astrophysical Journal, 648: L39–L42, 2006 September 1
© 2006. The American Astronomical Society. All rights reserved. Printed in U.S.A.

DETECTION OF A FAR-INFRARED BOW SHOCK NEBULA AROUND R HYA: THE FIRST MIRIAD RESULTS

T. Ueta,[1,2,3] A. K. Speck,[4] R. E. Stencel,[3] F. Herwig,[5] R. D. Gehrz,[6] R. Szczerba,[7] H. Izumiura,[8] A. A. Zijlstra,[9] W. B. Latter,[10] M. Matsuura,[11] M. Meixner,[12] M. Steffen,[13] and M. Elitzur[14]

Received 2006 June 9; accepted 2006 July 13; published 2006 August 10

ABSTRACT

We present the first results of the MIRIAD (MIPS InfraRed Imaging of AGB Dust shells) project using the *Spitzer Space Telescope*. The primary aim of the project is to probe the material distribution in the extended circumstellar envelopes (CSEs) of evolved stars and recover the fossil record of their mass-loss history. Hence, we must map the whole of the CSEs plus the surrounding sky for background subtraction while avoiding the central star that is brighter than the detector saturation limit. With our unique mapping strategy, we have achieved better than 1 MJy sr^{-1} sensitivity in 3 hr of integration and successfully detected a faint (<5 MJy sr^{-1}), extended (~400″) far-infrared nebula around the asymptotic giant branch (AGB) star R Hya. Based on the parabolic structure of the nebula, the direction of the space motion of the star with respect to the nebula shape, and the presence of extended Hα emission cospatial to the nebula, we suggest that the detected far-IR nebula is due to a bow shock at the interface of the interstellar medium and the AGB wind of this moving star. This is the first detection of the stellar-wind bow shock interaction for an AGB star and exemplifies the potential of *Spitzer* as a tool to examine the detailed structure of extended far-IR nebulae around bright central sources.

Subject headings: circumstellar matter — infrared: stars — ISM: structure — stars: AGB and post-AGB — stars: individual (R Hydrae) — stars: mass loss

1. INTRODUCTION

Evolved stars of intermediate initial mass (~1–8 $M_\odot$) are major contributors to the interstellar medium (ISM). However, the mechanism by which the ISM is enriched is not well understood. The circumstellar envelopes (CSEs) of evolved stars, asymptotic giant branch (AGB) and post-AGB stars in particular, contain the fossil record of their mass-loss history and therefore have the potential to verify many aspects of stellar evolution. *IRAS* and *ISO* data indicated that parsec-sized dusty CSEs exist around these infrared (IR) objects (e.g., Young et al. 1993). Moreover, these large CSEs show evidence for mass-loss variations that correlate with evolution of the star (e.g., Speck et al. 2000).

Previous observations lacked the sensitivity and spatial resolution to investigate the full extent and structure of these large dusty CSEs. Using the unique sensitivity and mapping capabilities of the Multiband Imaging Photometer for *Spitzer* (MIPS; Rieke et al. 2004) on board the *Spitzer Space Telescope* (Werner et al. 2004), we have been conducting far-IR imaging observations to probe the material distribution in the extended CSEs around several evolved stars. Our maps are the deepest yet and have the most complete spatial coverage, allowing the most detailed study into the CSE structure to date.

In this Letter, we report the first results of the MIPS IR Imaging of AGB Dust shells (MIRIAD) project (program ID 20258) for the AGB star R Hya. This star is a Mira variable well known for its decreasing period (Zijlstra et al. 2002) and the presence of a detached CSE (Young et al. 1993; Hashimoto & Izumiura 1997; Hashimoto et al. 1998). Below we describe the observations in § 2 and data reduction in § 3, and we present the results and discussion in § 4.

2. OBSERVATIONS

We observed R Hya at 70 and 160 μm using *Spitzer* MIPS on 2006 February 26 as part of the MIRIAD project. R Hya was the first target for which we obtained data in both of the MIPS Ge bands. We mapped a roughly square region (24′ × 24′) at 70 μm and a nearly linear region (24′ × 2.′4) at 160 μm, while avoiding the central region (2′ × 1′ and 1.′5 × 2′ at 70 and 160 μm, respectively), using exposures in photometry/fixed-cluster-offset mode. The MIRIAD maps can cover the entire target CSEs plus enough surrounding sky for background subtraction. Care was taken to avoid the central star that is brighter than the saturation limit of the MIPS arrays. Figure 1 visualizes the sky coverage.

The 70 μm observations consisted of three Astronomical Observation Requests (AORs), which sequentially covered the outer, mid, and inner regions of the CSE. To maximize the dynamic range, we used progressively longer exposure times for regions farther away from the central star: per pixel, per data collection event (DCE) exposure times were 18.87, 62.91, and 251.66 s for the inner, mid, and outer regions, respectively. The "gap" in the 70 μm sky coverage (along the in-scan direction toward the south of the central star; Fig. 1) is unavoid-

[1] NASA Ames Research Center/USRA SOFIA Office, MS 211-3, Moffett Field, CA 94035; tueta@sofia.usra.edu.
[2] NRC Research Associate/NASA Postdoctoral Program Research Fellow.
[3] Department of Physics and Astronomy, University of Denver, Denver, CO 80208.
[4] Department of Physics and Astronomy, University of Missouri, Columbia, MO 65211.
[5] Theoretical Astrophysics Group, LANL, Los Alamos, NM 87545.
[6] Department of Astronomy, University of Minnesota, Minneapolis, MN 55455.
[7] N. Copernicus Astronomical Center, Rabiańska 8, 87-100 Toruń, Poland.
[8] Okayama Astrophysical Observatory, National Astronomical Observatory, Kamogata, Asakuchi, Okayama 719-0232, Japan.
[9] University of Manchester, School of Physics and Astronomy, P.O. Box 88, Manchester M60 1QD, UK.
[10] NHSC, MC 100-22, Caltech, Pasadena, CA 91125.
[11] National Astronomical Observatory, Mitaka, Tokyo 181-8588, Japan.
[12] STScI, 3700 San Martin Drive, Baltimore, MD 21218.
[13] Astrophysikalisches Institut Potsdam, An der Sternwarte 16, 14482 Potsdam, Germany.
[14] Physics and Astronomy Department, University of Kentucky, Lexington, KY 40506.

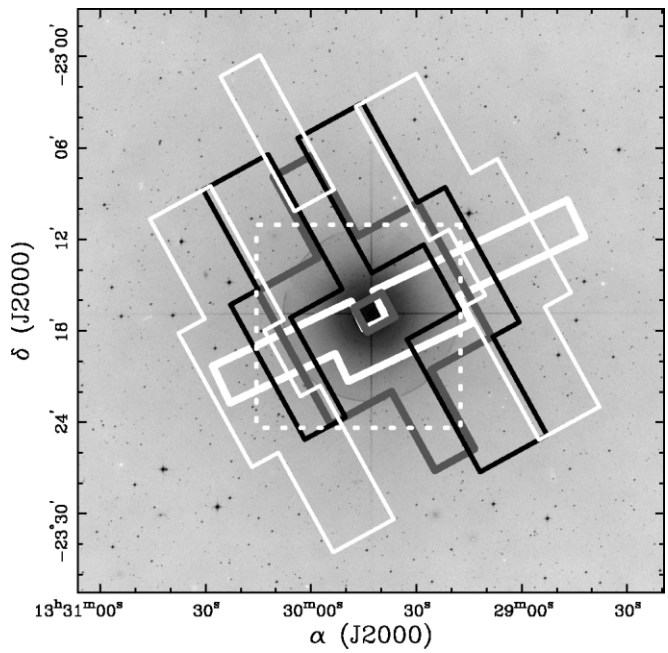

FIG. 1.—MIRIAD sky coverage over R Hya at 160 μm (*thick white line*) and at 70 μm for the outer (*thin white line*), intermediate (*black line*), and inner (*gray line*) regions. The "gap" to the south of the star is unavoidable to prevent the central star from falling into the 24 μm array. The central box (*dashed white line*) delineates the field of view of Fig. 2. The gray-scale SERC-I plate image (at 790 nm) was taken from the Digitized Sky Surveys.

able because the central star would fall onto the 24 μm array when the 70 μm aperture covers this region.

The 160 μm offsetting was done by a single AOR so that the linear map was swept in both the forward and backward directions along the cross-scan direction. To maximize the dynamic range, we repeated exposures at and near both ends of the linear map: per pixel exposure times are 167.76, 251.56, and 335.52 s depending on the number of repeats. Our observing scheme is also summarized in Table 1.

3. DATA REDUCTION

We initially constructed mosaicked maps from the pipeline-calibrated Basic Calibrated Data (BCD) products using the Mosaicker software (ver. 093005) provided by the *Spitzer* Science Center (SSC 2005).[15] However, the BCD-mosaicked maps were affected by detector artifacts. The effects were especially severe in the 70 μm map, in which the "streaking" (due to residual variations of the slow response of the detector as a function of time) was rampant and worsened increasingly toward the end of the observing sequence, probably because residual cosmic-ray charge slowly built up in the detector.

Hence, we performed a custom data reduction from the raw data. First, we used the latest Ge Reprocessing Tools (GeRT) software (ver. 041506 of S14 processing)[16] to create our own BCDs. The most important step in custom BCD generation is to do proper stimulator-flash (stim) calibration (Gordon et al. 2005). For the data from the mid and outer AORs at 70 μm, for which most of the emission is of sky (the zodiacal light, ISM, and cosmic IR background), the best results were produced from stim calibrations with piecewise linear fitting excluding stim frames on the nearby point sources. For the data from the inner region at 70 μm, for which most of the field can be bright by the central star and CSE emission, the best outcome was yielded from calibrations with spline fitting using all the raw data. For the 160 μm data, for which emission is of both sky and nonsky, the best results were obtained from stim calibrations with piecewise linear fitting using all the raw data.

For each BCD pixel, we followed the time evolution of pixel values and performed a linear least-squares fit using only the "sky" values to determine the baseline for sky subtraction. We tested this baseline fitting on the pixel, column, and column-of-4-pixel (readout is done for four columns at a time) bases, and the pixel basis fitting yielded the best results. This process worked especially well in removing linear streakings in the 70 μm maps that resulted from the column-dependent responsivity and the relatively linear way in which photometry-mode mapping scans across the sky.

However, the data obtained from the last offset position at 70 μm showed some residual column-dependent artifacts. This probably occurred because the detector responsivity had been compromised by the brightest region of the field near the central star scanned immediately before the end of the observing sequence (i.e., the detector is due for annealing). The remaining artifacts were removed by flat-fielding all the frames taken at the last offset position using their median frame.

After the baseline fitting, we subtracted the derived sky value at the time of exposure from the entire data set on pixel basis. The subtracted sky values were 13.9, 14.4, and 15.5 MJy sr^{-1}, respectively, for the outer, mid, and inner regions at 70 μm and 19.0 MJy sr^{-1} at 160 μm. The increasing sky value with decreasing aperture at 70 μm illustrates the need of baseline determination far enough away from the central object. We adopted 13.9 MJy sr^{-1} as the 70 μm sky emission, and the difference was added back to the BCDs for the mid and inner regions (0.5 and 1.6 MJy sr^{-1}, respectively) to compensate for the oversubtraction. The expected sky emission, obtained by the Spot Software,[17] is 11.5 and 14.2 MJy sr^{-1} at 70 and 160 μm, respectively. This step was done by our own IDL script.

Finally, the custom-processed BCDs were mosaicked together using the Mosaicker while cosmic rays were removed. The resulting maps still showed some structure intrinsic to the diffraction spikes of the point-spread function (PSF), especially

[15] See http://ssc.spitzer.caltech.edu/postbcd.

[16] See http://ssc.spitzer.caltech.edu/mips/gert.

[17] See http://ssc.spitzer.caltech.edu/propkit/spot.

TABLE 1
SUMMARY OF *SPITZER*/MIRIAD OBSERVATIONS OF R HYA

Band	AOR Key	Start Time	Image Scale (arcsec)	Field Size	Exposure (s)	Cycle	Integration[a] (s)	Offsets	DCE Counts	Total Duration (s)
70 μm (outer)	14472448	2006 Feb 26 07:15:03	9.84	Large	10	2	125.83	13	418	6493
70 μm (mid)	14472704	2006 Feb 26 08:59:52	9.84	Large	10	1	62.91	8	145	2625
70 μm (inner)	14472960	2006 Feb 26 09:40:12	9.84	Large	3	1	18.87	6	109	1204
160 μm	14472192	2006 Feb 26 04:20:36	16.0	Small	10	2	83.88	22	792	10256

[a] Integration times are per pixel per DCE in "real" seconds.

TABLE 2
SUMMARY OF MEASUREMENTS AND MAP CHARACTERISTICS

Band	Flux (Jy)		Sky, σ (MJy sr^{-1})				Coverage (pixel^{-1})	
	CSE[a]	Star[b]	Sky	σ_{avg}	σ_{best}	σ_{est}[c]	Avg	Best
70 μm (mosaic)	19.4 ± 3.6	33.9	13.9	0.47	0.15	...	7	45
70 μm (outer)	...	...	13.9	0.56	0.16	0.26	5	45
70 μm (mid)	...	...	14.4	0.68	0.21	0.37	3	24
70 μm (inner)	...	...	15.5	0.86	0.28	0.68	2	17
160 μm	5.8 ± 1.3	4.5	19.0	0.31	0.12	0.38	15	80

[a] Lower limit.
[b] Based on the scaled PSF/PRF maps.
[c] 1 σ sensitivity estimated with the SENS-PET tool.

at 70 μm. Thus, we used the *Spitzer* TinyTim (STinyTim) software[18] to create simulated point-response function (PRF) maps (with the $F_\nu \propto \nu^2$ emissivity assumption) and subtracted them from the mosaicked maps by scaling flux within an annulus around the central unobserved region.

The resulting maps are in 4″.92 and 7″.99 pixel^{-1} (subpixelized from the nominal scale by a factor of 2) with the average of seven and 15 sky coverages per pixel and the maximum of 45 and 80 sky coverages per pixel at 70 and 160 μm, respectively. At least four sky coverages are achieved in 88% and 94% of the mapped area at 70 and 160 μm, respectively, to fulfill the minimum level of redundancy. The resulting 1 σ sensitivities are consistent with the performance estimates done by the SENS-PET tool[19]: we have achieved the required sensitivity level of 1 MJy sr^{-1} as planned. Characteristics of the resulting maps are listed in Table 2.

4. RESULTS AND DISCUSSION

Figure 2 shows the background/PRF-subtracted, mosaicked MIPS color maps of R Hya at 70 μm (*top left*) and 160 μm (*top middle*), which clearly display faint, extended emission.

[18] See http://ssc.spitzer.caltech.edu/archanaly/contributed.

[19] See http://ssc.spitzer.caltech.edu/tools/senspet.

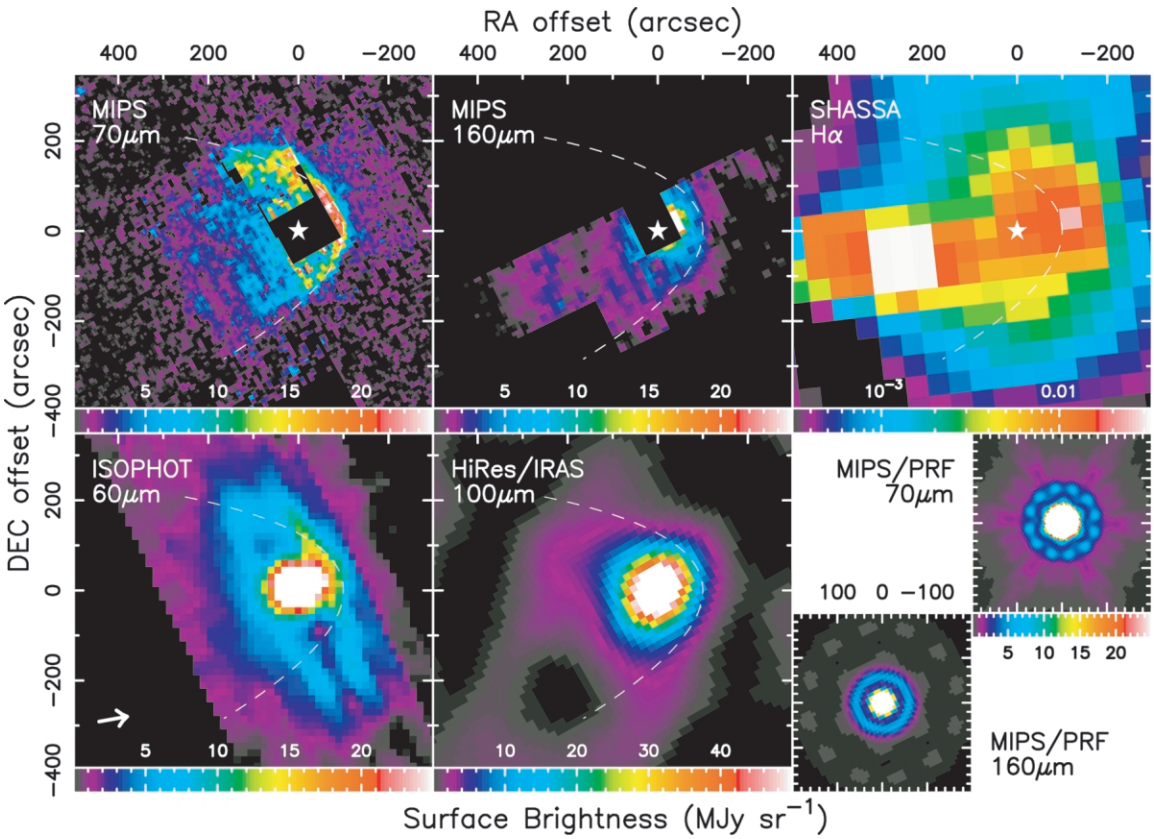

FIG. 2.—Background/PRF-subtracted, mosaicked MIPS maps of R Hya (north is up, and east is to the left) at 70 μm (*top left*) and 160 μm (*top middle*). For comparison, an ISOPHOT PHT32 map at 60 μm (*bottom left*), a HiRes-processed *IRAS* map at 100 μm (*bottom middle*), a SHASSA Hα map (*top right*), and STinyTim PRF maps (*bottom right*) are also shown. The images are zeroed at the position of R Hya ($[\alpha, \delta]_{J2000.0} = [13^h29^m42^s.7803, -23°16'52''.792]$; Perryman et al. 1997). The position of the star is indicated by the star. The tick marks indicate the angular offsets in arcseconds. Linear color scaling of surface brightness (in MJy sr^{-1}) is shown at the bottom of each panel. A parabolic curve $y = x^2/3l$, which closely represents the stellar-wind bow shock near the apex, is displayed by the dashed lines. The arrow at the bottom left corner shows the direction of the proper motion of the star, (−60.73, 11.01) mas yr^{-1}.

Also shown are a pipeline-processed ISOPHOT PHT32 map at 60 μm (*bottom left*; Hashimoto & Izumiura 1997),[20] a HiRes-processed *IRAS* map at 100 μm (*bottom middle*),[21] an Hα map (*top right*) from the Southern Hα Sky Survey Atlas[22] (SHASSA; Gaustad et al. 2001), and STinyTim PRF maps at 70 and 160 μm (*bottom right*).

The 70 μm map shows an arclike surface brightness distribution at >10 MJy sr^{-1} surrounded by even fainter emission (<10 MJy sr^{-1}) of ∼400″ diameter. The arc structure appears parabolic with the apex pointed toward the west-northwest direction: the distance to the apex from the central star is 100″ (see below). While the southern part of the arc remains physically thin (∼40″), the northern part becomes wider (∼100″). The width of the parabola at the tail end is about 370″. The brightest region near the apex of the parabolic arc (of ∼20 MJy sr^{-1}) can also be seen in the ISOPHOT 60 μm map. In retrospect, the ISOPHOT map appears to have captured most of the arc to the north, in spite of the instrumental artifacts.

The 160 μm map also displays an extended nebulosity along the arc (<5 MJy sr^{-1}), which appears consistent with the 100 μm HiRes/*IRAS* map as well as the 100 μm high-resolution *IRAS* map based on the pyramid maximum entropy method (Hashimoto et al. 1998). There is a bright spot near the northwest edge of the central unobserved region (at ∼45″ from the star), which does not spatially correspond to the 70 μm arc. It is probably caused by the near-IR light leak at 160 μm (SSC 2005; for R Hya, $m_J = -1.3$ mag and $F_{160\,\mu m}/F_{2\,\mu m} = 0.0006$).

The integrated flux over the entire nebula is 19.4 ± 3.6 and 5.8 ± 1.3 Jy at 70 and 160 μm, respectively. These values are the lower limits since there are no data in the central unobserved region. From the scaled PRFs, the stellar fluxes at 70 and 160 μm are estimated to be 33.9 and 4.5 Jy, respectively.

Van Buren & McCray (1988) have found parabolic far-IR nebulae around hot stars and attributed some of them to bow shocks at the interface between the stellar wind and ISM around a moving star. R Hya is known to have the proper motion of (−60.73, 11.01) mas yr^{-1} (Perryman et al. 1997) toward the apex of the arc as indicated by the bottom left arrow in Figure 2. Moreover, the shape of the far-IR arc closely follows the curve $y = x^2/3l$ (where l is the distance between the apex and star), which has been shown numerically to represent the apex shape of the stellar-wind bow shock by Mac Low et al. (1991), as delineated by the dashed lines in Figure 2. Furthermore, Hα emission is extended along the parabolic apex and axis, showing the presence of ionized gas in these regions.

Therefore, we attribute the parabolic far-IR nebula around R Hya to shock-excited line emission (such as [O I] 63 and 146 μm) and locally heated dust emission arising from a stellar-wind bow shock interface between the ISM and the swept-up AGB wind of this moving star. This is the first detection of the stellar-wind bow shock interaction for an AGB star and is a surprise discovery, given our original aim of the study. Nevertheless, our results exemplify the potential of *Spitzer* as a tool to examine the far-IR structure of extended emission around the bright central object. A follow-up IR spectroscopy can determine the emission characteristics.

At 165 pc (Zijlstra et al. 2002) with the −10 km s^{-1} radial velocity (Knapp et al. 1998), the space velocity of R Hya is 50 ± 1 km s^{-1} into the direction 12° away (receding side) from the plane of the sky. The asymmetric CO profiles (Knapp et al. 1998; Teyssier et al. 2006) can then be explained by this inclined bow shock, in which the receding and approaching shock fronts intersect with the line of sight at distinct angles.

The physical dimensions of the observed bow shock (0.03 pc thick located at 7.9 × 10^{-2} pc ahead of the star) are consistent with the stellar-wind bow shock models for AGB stars (Wareing et al. 2006a). Adopting the mass-loss rate of 3 × 10^{-7} $M_\odot$ yr^{-1} (Zijlstra et al. 2002), wind velocity of 10 km s^{-1} (e.g., Knapp et al. 1998), and formula for l derived from the momentum conservation across the shock (Van Buren et al. 1990, eq. [2]), the ambient H density is 0.4 cm^{-3} and the shock surface density is 2.5 × 10^{-7} g cm^{-2}. Thus, the estimated amount of matter contained in the bow shock is about 1.3 × 10^{-4} $M_\odot$, assuming a paraboloidal bow shock of $y = x^2/3l$ with a 300″ opening radius.

The MIPS maps indicate the presence of matter in the downstream (emission at ∼3 MJy sr^{-1} up to 300″ away, which is corroborated by the Hα map). The downstream emission may arise from a tail of a steady state bow shock that is formed by ram pressure stripping from the head of the shock (Wareing et al. 2006a). The local emission peaks at ∼250″ away in the downstream may correspond to vortices that results from instabilities in the downstream flow shed off from the bow shock (C. J. Wareing 2006, in preparation). Modeling of the bow shock nebula of R Hya will be presented by Wareing et al. (2006b).

This work is based on observations made with the *Spitzer Space Telescope*, which is operated by the JPL/Caltech under a contract with NASA. Support for this work was provided by NASA through an award issued by JPL/Caltech. We also acknowledge additional support for the following individuals: an NPP Research Fellowship Award to T. Ueta, NASA ADP grant NAG 5-12675 to A. K. Speck, the LDRD program (20060357ER) at LANL for F. Herwig, NASA contract 1215746 issued by JPL/Caltech to R. D. Gehrz, grant 2.P03D.017.25 to R. Szczerba, a Grant-in-Aid (C) from JSPS (17540221) to H. Izumiura, JSPS for M. Matsuura, and NSF grant AST 05-07421 to M. Elitzur. We thank C. J. Wareing for sharing his insights on the stellar-wind bow shocks with us.

[20] See http://www.iso.vilspa.esa.es.
[21] See http://irsa.ipac.caltech.edu/IRASdocs/hires_over.html.
[22] See http://amundsen.swarthmore.edu/SHASSA.

REFERENCES

Gaustad, J. E., McCullough, P. R., Rosing, W., & Van Buren, D. 2001, PASP, 113, 1326
Gordon, K. D., et al. 2005, PASP, 117, 503
Hashimoto, O., & Izumiura, H. 1997, Ap&SS, 255, 349
Hashimoto, O., Izumiura, H., Kester, D. J. M., & Bontekoe, Tj. R. 1998, A&A, 329, 213
Knapp, G. R., Young, K., Lee, E., & Jorissen, A. 1998, ApJS, 117, 209
Mac Low, M.-M., Van Buren, D., Wood, D. O. S., & Churchwell, E. 1991, ApJ, 369, 395
Perryman, M. A. C., et al. 1997, A&A, 323, L49
Rieke, G., et al. 2004, ApJS, 154, 25
Speck, A. K., Meixner, M., & Knapp, G. R. 2000, ApJ, 545, L145
Spitzer Science Center. 2005, *Spitzer* Observers' Manual, Ver. 6.0 (Pasadena: SSC), http://ssc.spitzer.caltech.edu/documents/som/
Teyssier, D., Hernandez, R., Bujarrabal, V., Yoshida, H., & Phillips, T. G. 2006, A&A, 450, 167
Van Buren, D., Mac Low, M.-M., Wood, D. O. S., & Churchwell, E. 1990, ApJ, 353, 570
Van Buren, D., & McCray, R. 1988, ApJ, 329, L93
Wareing, C. J., et al. 2006a, MNRAS, 366, 387
———. 2006b, MNRAS, in press
Werner, M. W., et al. 2004, ApJS, 154, 1
Young, K., Phillips, T. G., & Knapp, G. R. 1993, ApJS, 86, 517
Zijlstra, A. A., Bedding, T. R., & Mattei, J. A. 2002, MNRAS, 334, 498